



Synthesis and optimization of spherical nZVI (20–60 nm) immobilized in bio-apatite-based material for efficient removal of phosphate: Box-Behnken design in a fixed-bed column

Mohammad Javad Amiri¹

Received: 16 December 2021 / Accepted: 27 April 2022 / Published online: 6 May 2022
© The Author(s), under exclusive licence to Springer-Verlag GmbH Germany, part of Springer Nature 2022

Abstract

In the present study, bio-apatite/nZVI composite was synthesized through Fe(III) reduction with sodium borohydride and was fully characterized by FTIR, XRD, SEM–EDX, TEM, BET, BJH, and pH_{PZC} . Column experiments were carried out for the removal of phosphate as a function of four operational parameters including initial phosphate concentration (100–200 mg L^{-1}), initial solution pH (2–9), bed height (2–6 cm), and influent flow rate (2.5–7.5 mL min^{-1}) using a response surface methodology (RSM) coupled with Box-Behnken design (BBD). 2D contour and 3D surface plots were employed to analyze the interactive effects of the four operating parameters on the column performance (e.g., uptake capacity and saturation time). According to ANOVA analysis, the influent flow rate and bed height are the most important factor on phosphate uptake capacity and saturation time, respectively. A quadratic polynomial model was excellently fitted to experimental data with a high coefficient of determination (> 0.96). The RSM-BBD model predicted maximum phosphate adsorption capacity of 85.71 mg g^{-1} with the desirability of 0.995 under the optimal conditions of 135.35 mg L^{-1} , 2, 2 cm, and 7.5 mL min^{-1} for initial phosphate concentration, initial solution pH, bed height, and influent flow rate, respectively. The XRD analysis demonstrated that the reaction product between bio-apatite/nZVI composite and phosphate anions was $\text{Fe}_3(\text{PO}_4)_2 \cdot 8\text{H}_2\text{O}$ (vivianite). The suggested adsorbent can be effectively employed up to five fixed-bed adsorption–desorption cycles and was also implemented to adsorb phosphate from real samples.

Keywords Operational parameters · Interactive effects · Quadratic model · Desirability · Vivianite

Introduction

Phosphorus in various species of orthophosphates, metaphosphates, and polyphosphates has been detected in the water resources (Arshadi et al. 2015a). Industrial and municipal wastewater as the point sources and agricultural drainage as the non-point sources constitute phosphate pollution in surface water and shallow groundwater (Almeelbi and Bezbaruah 2012). The high concentration level of phosphate causes eutrophication, which reduces dissolved oxygen, resulting in fish death and destroying aquatic ecosystem (Almeelbi and Bezbaruah 2012). The recommended discharge level of

phosphorous into surface waters is 0.5 to 1 mg L^{-1} according to WHO (Malakootian et al. 2018). Therefore, elimination of excess phosphates from wastewater is essential to barricade eutrophication phenomenon.

Among different conventional and modern technologies for phosphate removal from wastewater, adsorption by nano zero-valent iron (nZVI) has received a great deal of attention due to its high efficiency, high surface/volume ratios, short adsorption time, and applicability for in situ and ex situ remediation (Almeelbi and Bezbaruah 2012; Wu et al. 2013; Wen et al. 2014; Arshadi et al. 2015a, b, 2018; Maamoun et al. 2018). On the other hand, trapping of nZVI particles in porous material is one of the most promising technique to increase the dispersibility of nanoparticles and also prevent their agglomeration in environmental remediation (Eslamian et al. 2013). As a result, different beads such as sinigue-las (Arshadi et al. 2015b), cellulose filter paper (Arshadi et al. 2018), sepiolite (Malakootian et al. 2018), activated carbon (Singh and Singh 2018), and rape straw biochar (Ma

Responsible Editor: Angeles Blanco

✉ Mohammad Javad Amiri
mj_amiri@fasau.ac.ir

¹ Department of Water Engineering, Faculty of Agriculture, Fasa University, Fasa 74616-86131, Iran

et al. 2020) were successfully used for supporting nZVI in phosphate removal. To the best of our knowledge, a few papers have been published on phosphate removal by stabilized nZVI, particularly by bio-apatite-based materials. In our previous studies, the bio-apatite-based adsorbent was produced via the combustion of ostrich bone wastes under ambient conditions (Amiri et al. 2013, 2019), and satisfactorily applied to eliminate heavy metals. Unfortunately, the recovery and reuse of bio-apatite-based material are difficult. As a result, nZVI particles can be combined with bio-apatite-based materials to increase their separation in wastewater treatment. In this regard, the nZVI particles were synthesized through the chemical reduction of $\text{FeCl}_3 \cdot 6\text{H}_2\text{O}$ using sodium borohydride and supported by bio-apatite-based material to enhance its stability in ambient conditions. The obtained composite was satisfactorily applied in removing heavy metals from batch (Gil et al. 2018) and column experiments (Amiri et al. 2017, 2018b).

Column studies require a large number of expensive and time-consuming experimental runs to acquire the optimal adsorption conditions for maximizing removal percentage of the target pollutants (Gu et al. 2018). Response surface methodology (RSM) as a combination of statistical and mathematical tools have been successfully applied for optimization and interaction analysis of adsorption operating parameters in the batch (Srivastava et al. 2015; Bahrami et al. 2019; Amiri et al. 2018a, 2019) and column (Liu et al. 2016; Roy et al. 2017; Gu et al. 2018) modes. Moreover, predicting target contaminant removal using the second-order polynomial equation as well as the sensitivity analysis can be accomplished by RSM.

In this paper, bio-apatite/nZVI composite was satisfactorily applied to eliminate phosphate from simulated wastewater, and the effect of some relevant parameters such as flow rate, initial concentration, pH, and bed depth was optimized in a fixed-bed column using RSM coupled with Box-Behnken design (BBD). Hence, RSM-BBD was employed as a versatile tool to analyze the independent and cumulative effects of operating parameters for maximizing phosphate removal capacity. Furthermore, a second-order polynomial equation as well as analysis of variance (ANOVA) are proposed to reveal the detailed interactions. Finally, the possible mechanisms of phosphate elimination by bio-apatite/nZVI composite were investigated using a combination of column experiments and characterization results.

Material and methods

Materials

High purity (99%) of monopotassium phosphate (KH_2PO_4) purchased from Sigma-Aldrich Co. was used as a source

of phosphate. Phosphate stock solution was provided by dissolving a given mass of KH_2PO_4 in 1000 mL of deionized water and diluted for working solutions. Other reagents including ferric chloride hexahydrate ($\text{FeCl}_3 \cdot 6\text{H}_2\text{O}$, 98%), sodium borohydride (NaBH_4 , 98%), sodium hydroxide (NaOH , 98%), methanol (CH_3OH , 99.9%), and hydrochloric acid (HCl , 37%) were obtained from Sigma-Aldrich Co. and applied without further purification.

Synthesis of bio-apatite/nZVI composite

The bio-apatite/nZVI composite was synthesized using the liquid-phase reduction method according to the procedure presented by Zhang et al. (2011), with some modifications. At first, an appropriate amount of ostrich bone waste was converted to hydroxyapatite ($\text{Ca}_{10}(\text{PO}_4)_6(\text{OH})_2$) by a thermal treatment using annealing at 550 °C for 24 h under air conditions and denoted as the bio-apatite material (Amiri et al. 2013). Then, 4 g of the bio-apatite material and 10 g of $\text{FeCl}_3 \cdot 6\text{H}_2\text{O}$ were dissolved into 100 mL of ethanol and deionized water in a 4:1 (v/v) ratio (Fig. 1). After stirring for 30 min on the heater by electric rod stirrer, NaBH_4 solution (1.8 g per 100 mL) was added dropwise (20–30 drops/min) while stirring regularly under inert nitrogen gas for another 20 min. Subsequently, the resulting solution became black

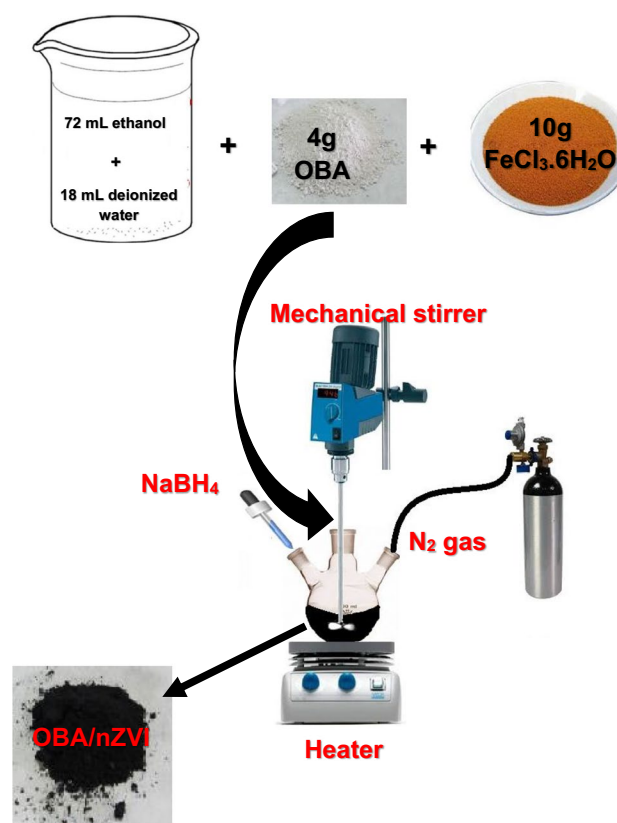
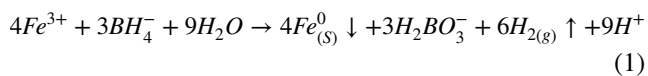


Fig. 1 Schematic diagram for OBA/nZVI synthesis

and bio-apatite/nZVI particles were formed (Fig. 1). The NaBH_4 reduction reaction can be expressed as follows:



The bio-apatite/nZVI particles were vacuum filtrated from the solution through Whatman filter paper No. 1 and washed frequently with 99% absolute ethanol to eliminate residual Cl and B. Finally, the particles were dried under inert nitrogen gas.

Characterization techniques

A scanning electron microscope combined with an energy dispersive X-ray (SEM–EDX, TESCAN-Vega 3, USA) was employed to examine the surface morphology and the chemical composition of the bio-apatite /nZVI composite. A high-resolution transmission electron microscope (TEM, Zeiss-EM10C, Germany) at 100 kV acceleration voltages was used to study the morphological analysis and compositional characteristics of adsorbent. An X-ray diffraction analysis apparatus (XRD, Bruker D8 Advance, Germany) with Cu-K α radiation ($\lambda = 0.154$ nm) in the 2θ range of 10–100° at 40 kV/100 mA was employed to investigate the crystalline phase structures of the bio-apatite/nZVI composite. A Fourier transform infrared spectroscopy (FTIR, PerkinElmer Spectrum two, USA) was used to verify the functional groups of the bio-apatite/nZVI composite before and after mixing with phosphate in the range of 400–4000 cm^{-1} . A zeta potential meter (Zetasizer Nano ZS90, Malvern, UK) was employed to determine the isoelectric point of the bio-apatite/nZVI composite. The N_2 adsorption–desorption isotherms at a relative pressure of 0.98 and temperature of 77 K (Belsorp mini II instrument, Japan) were used to determine the total pore volume, pore size distribution, and BET surface area of the bio-apatite /nZVI composite.

Column experiments

The dynamic adsorption of the phosphate was adapted in a packed-bed column made from glass with an inside diameter of 2 cm and a height of 20 cm. Two glass-ball layers were considered to support the bio-apatite/nZVI composite for the prevention of the loss of the adsorbent in effluent flow (Fig. S1). The known amounts of the bio-apatite/nZVI composite were placed in the column to achieve an equivalent bed height of 2, 4, or 6 cm. Before beginning the test, the adsorbent was washed with deionized water. Then, phosphate solutions with initial concentrations of 100, 150, or 200 mg L^{-1} and pH amounts of 2, 5.5, or 9 were transported upward into the column using a peristaltic pump at room temperature with feed flow rates of 2.5, 5, or 7.5 mL min^{-1} . The outflow samples were gathered at regular time intervals until the outlet

phosphate concentration was approximately equal to the inlet concentration. The residual phosphate concentration was analyzed by the molybdenum-blue ascorbic acid method (Rice et al. 2017) using UV–Vis spectrophotometry (Shimadzu UV/vis 2100, Japan) at 690 nm.

Column data analysis

The column performance was assessed in terms of equilibrium uptake capacity of phosphate at the total flow time (q_{eq}), as well as the saturation time (t_s). These parameters (q_{eq} and t_s) were acquired from the breakthrough curves (BTC), as described by plotting the C_t/C_o versus time (Yun 2000), where C_t is the effluent phosphate concentration at time t and C_o is the influent phosphate concentration. The saturation time (t_s) is related to the time that phosphate concentration in the outlet reached 90% of the initial phosphate concentration (Hu et al. 2020). The uptake capacity at the total flow time (q_{eq} , mg g^{-1}) is calculated according to Eq. (2) (Chowdhury and Saha 2013):

$$q_e = \frac{Q \times \int_{t=0}^{t=\text{total}} (C_o - C_t) dt}{(1000) M} \quad (2)$$

where C_o and C_t are the influent and effluent phosphate concentration (mg L^{-1}), respectively, Q is the flow rate (mL min^{-1}), t_{total} is the total flow time (min), and M represents the dry mass of bio-apatite/nZVI composite (Cavas et al. 2011).

RSM-BBD design

RSM-BBD design was used to model and optimize conditions of phosphate removal by bio-apatite/nZVI composite. Four independent factors consisting of initial phosphate concentration (100–200 mg L^{-1}), initial solution pH (2–9), bed height (2–6 cm), and influent flow rate (2.5–7.5 mL min^{-1}) were selected as the input of RSM-BBD and the uptake capacity of phosphate at the total flow time (q_{eq} , mg g^{-1}), as well as the saturation time (t_s , h) as the output. Table 1 presents the three levels (low, middle, and high) of independent factors. Overall, 27 experimental sets were designed by using Minitab software Version 16 (Table S1). The second-order polynomial equation was employed to correlate the output and input factors as follows (Gu et al. 2018; Mohammad et al. 2019):

$$Y = a_0 + \sum_{i=1}^n a_i x_i + \sum_{i=1}^n a_{ii} x_i^2 + \sum_{i=1}^n \sum_{j=i+1}^n a_{ij} x_i x_j \quad (3)$$

where Y is the estimated response (i.e., q_{eq} and t_s), a_0 , a_i , a_{ii} , and a_{ij} are the constant, linear, quadratic, and interaction regression coefficients, respectively, x_i and x_j are the independent factors corresponding to the initial phosphate concentration, initial solution pH, bed height, and influent flow rate. The coded value (X_i) and the real value (x_i) can be

Table 1 Experimental levels of four independent variables applied in design of experiment

Variables	Symbol	Level		
		Low (−1)	Middle (0)	High (+1)
Initial phosphate concentration (mg L ^{−1})	x_1	100	150	200
Initial solution pH	x_2	2	5.5	9
Bed height (cm)	x_3	2	4	6
Influent flow rate (mL min ^{−1})	x_4	2.5	5	7.5

related by the following equation (Maleki and Karimi-Jashni 2020):

$$X_i = \frac{x_i - x_0}{\Delta x} \quad (4)$$

where x_0 and Δx are the real value of the independent factor at the central point and the step-change in the real value, respectively. To assess the regression model and the importance of each independent variable, analysis of variance (ANOVA) was employed.

Mathematical models

Two well-known mathematical models consisting of the Thomas model and the bed depth service time (BDST) model were employed to describe the fixed-bed column adsorption data. The Thomas and BDST models in non-linear forms can be expressed by Eqs. (5) and (6), respectively (Cruz-Olivares et al. 2013; Bahrami et al. 2018).

$$\frac{C_t}{C_0} = \frac{1}{1 + \exp\left[\left(\frac{K_T}{Q}\right)(q_0 m - C_0 Q t)\right]} \quad (5)$$

$$\frac{C_t}{C_0} = \frac{1}{1 + \exp\left[K_{BD} C_0 \left(\frac{N_0}{C_0 U_0} L - t\right)\right]} \quad (6)$$

where K_T and K_{BD} is the Thomas and BDST rate constant [L (mg min)^{−1}], q_0 is the Thomas model adsorption capacity (mg g^{−1}), N_0 is the maximum adsorption capacity (mg L^{−1}), U_0 is the linear flow velocity (cm min^{−1}).

Results and discussion

Characterization of the adsorbent

The FTIR spectra analysis of the bio-apatite/nZVI composite was studied before and after phosphate adsorption in the range of 400–4000 cm^{−1} (Fig. 2a). The broad and strength peaks at 3500–3400 cm^{−1} of O–H groups was related to water adsorbed on the structure of the bio-apatite/nZVI composite (Amiri et al. 2016). The peaks at

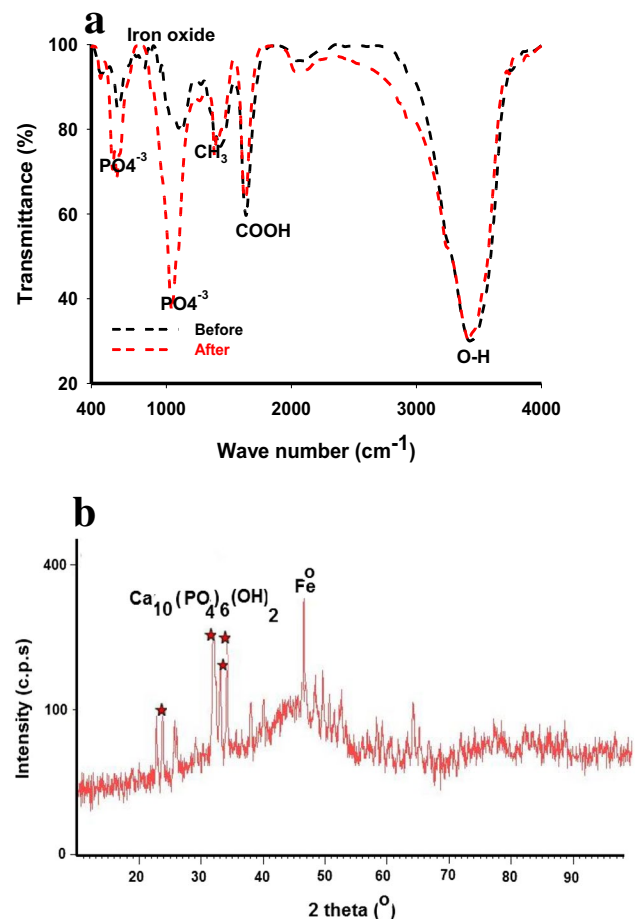


Fig. 2 FTIR analysis of the bio-apatite/nZVI composite before and after phosphate adsorption (a), and XRD analysis of sample (b)

960, 603 and 560 cm^{−1} were associated the P–O stretching vibration mode of the phosphate group (Zeng et al. 2019), whereas the band at 1040 cm^{−1} was characteristic of PO₄^{3−}, HPO₄^{2−}, and H₂PO₄[−] groups (Wu et al. 2013). A strong peak at 1742 cm^{−1} can be assigned to carboxyl groups and the peak at around 1433–1460 cm^{−1} is associated with –CH₃ bending vibration. Moreover, the small peak at 821 cm^{−1} is assigned to Fe–O stretching vibrations (Gil et al. 2018; Arshadi et al. 2015a). However, the FTIR spectrum of the bio-apatite/nZVI composite after interaction with phosphate solution shows that no new peaks formed during the

phosphate adsorption (Fig. 2a). An increase in absorbance peaks of the bio-apatite/nZVI composite at 1040, 960, 603, and 560 cm^{-1} introduce a phosphate group into adsorbent, forming the widest P-O group, which may be due to the electron-donating electrostatic interaction between the phosphate ions and the positive surface of adsorbent (Arshadi et al. 2015a, b). Also, a slight shift in the spectrum of the bio-apatite/nZVI composite after phosphate adsorption indicates that the interactions between the bio-apatite/nZVI composite and phosphate are based on hydrogen bonds (Ma et al. 2020; Amiri et al. 2020b).

The XRD pattern of the composite showed that Ca and P in the form of calcium hydroxyapatite ($\text{Ca}_{10}(\text{PO}_4)_6(\text{OH})_2$) at $2\theta = 25.81, 31.73, 32.91,$ and 34.52° as well as a strong peak at $2\theta = 45^\circ$, which clearly confirms the presence of nZVI particles, constitute the major components of the bio-apatite/nZVI composite (Fig. 2b).

The specific surface area, average pore diameter, and total pore volume of the composite were $109 \text{ m}^2 \text{ g}^{-1}$, 11 nm, and $0.31 \text{ cm}^3 \text{ g}^{-1}$, respectively. The bio-apatite/nZVI composite depicts mesoporosity structure according to the IUPAC classification because the diameter of the pores is between 2 and 50 nm. A comparison of the specific surface area of this work with those of literature such as $108.67 \text{ m}^2 \text{ g}^{-1}$ for carbon/nZVI composite (Crane and Scott 2014), $41.4 \text{ m}^2 \text{ g}^{-1}$ for ostrich bone waste- HNO_3 /nZVI composite (Arshadi et al. 2015a), $88.29 \text{ m}^2 \text{ g}^{-1}$ activated carbon/nZVI composite (Singh and Singh 2018), 72.77 for hydroxyapatite/nZVI composite (Zeng et al. 2019), and $34.23 \text{ m}^2 \text{ g}^{-1}$ for biochar/nZVI composite (Ma et al. 2020) shows that the used adsorbent behaves in a better way in all cases.

The isoelectric points (pH_{ZPC}) of the bio-apatite material, as well as the bio-apatite/nZVI composite before and after phosphate adsorption, are presented in Figure S2. As can be seen in Fig. S2, the pH_{ZPC} of bio-apatite material, bio-apatite/nZVI composite, and bio-apatite/nZVI composite after phosphate adsorption were 6.8, 5.8, and 4.65, respectively. At $\text{pH} < \text{pH}_{\text{ZPC}}$, the adsorbent surface was protonated and changed to positively charged, whereas at $\text{pH} > \text{pH}_{\text{ZPC}}$ the adsorbent surface was deprotonated and transformed to negatively charged. The shift of pH_{ZPC} from 6.8 to 5.8 indicates that the surface of the bio-apatite based material was chemically changed after modification and the nZVI was successfully immobilized on the adsorbent. In addition, the zeta potential of the bio-apatite/nZVI composite declined after phosphate adsorption with a remarkable shift of the pH_{ZPC} to a lower pH value due to the accumulation of negatively charged phosphate adsorbed on bio-apatite/nZVI composite (Fig. S2). Similar trend was observed by Li et al (2018).

Figure 3 indicates the surface morphology of the bio-apatite/nZVI composite that was analyzed by SEM and TEM. The original bio-apatite-based material are rod-like

structure, which was loaded with numerous nanoparticles (Fig. 3a). As can be seen in Fig. 3a, nZVI particles were dispersed well on the surface of the bio-apatite based material without any aggregation and were successfully attached to the beads. In fact, the bio-apatite-based material solved the poor mechanical strength, aggregation, oxidation, and low durability of bare nZVI (Arshadi et al. 2015a; Gil et al. 2018). The black ball-shaped in TEM images (Fig. 3b and c) was assigned to the anchored nZVI on the surface of bio-apatite-based material. The nZVI particles had a rough surface with a round shape ranging from 20 to 60 nm, which were very different from the chain-like structure of bare nZVI. The EDX spectrum of the bio-apatite/nZVI composite provides evidence for the presence of Ca, P, Fe, O, and Na as the major elements (Fig. S3). The signal of Ca, P, and Na came from the bio-apatite-based material, whereas the signal of Fe would come from nZVI particles. However, the element O would come from nZVI particles and the bio-apatite-based material.

Adsorption studies using RSM-BBD design

RSM-BBD design was used to evaluate the individual and interactive effects of initial phosphate concentration (x_1), initial solution pH (x_2), bed height (x_3), and influent flow rate (x_4), as the independent process factors on the uptake capacity of phosphate at the total flow time (q_{eq}), as well as the saturation time (t_s). In this regard, 27 designed column runs of the experimental conditions along with their results are represented in Table S1. According to results from Table S1, a quadratic polynomial model between responses and the process factors was developed for the coded values by the software.

$$t_s = 14.5 - x_1 - 2.5 x_2 + 3.83 x_3 - 1.83 x_4 + 1.67(x_1)^2 - 1.083 (x_2)^2 + 0.0417(x_3)^2 + 0.0417(x_4)^2 - 0.5(x_3x_4) \quad (7)$$

$$q_{\text{eq}} = 39.96 + 10.46x_1 - 7.73x_2 - 11.74 x_3 + 15.5 x_4 - 0.676 (x_1)^2 - 3.62 (x_2)^2 + 6.21 (x_3)^2 - 1.78 (x_4)^2 - 1.83 (x_1x_2) - 2.14 (x_1x_3) + 3.44 (x_1x_4) + 5.05(x_2x_3) - 3.78 (x_2x_3) - 6.43(x_3x_4) \quad (8)$$

Analysis of variance (ANOVA) was employed to determine the significance of the regression model for q_{eq} (Table 2) and t_s (Table S2). The significance of the values of the regression model for q_{eq} and t_s was evaluated by p -value, F -value, sum of the squares, standard deviation, “Lack of Fit”, R^2 , adjusted R^2 , predicted R^2 , and predicted residual error sum of squares (PRESS). A large amount of F -value implies the adequacy of RSM-BBD fits, whereas p -values lower than 0.05 show the significance of the regression coefficients (Maleki and Karimi-Jashni 2020). According

Fig. 3 SEM (a) and TEM (b and c) images of the bio-apatite/nZVI composite

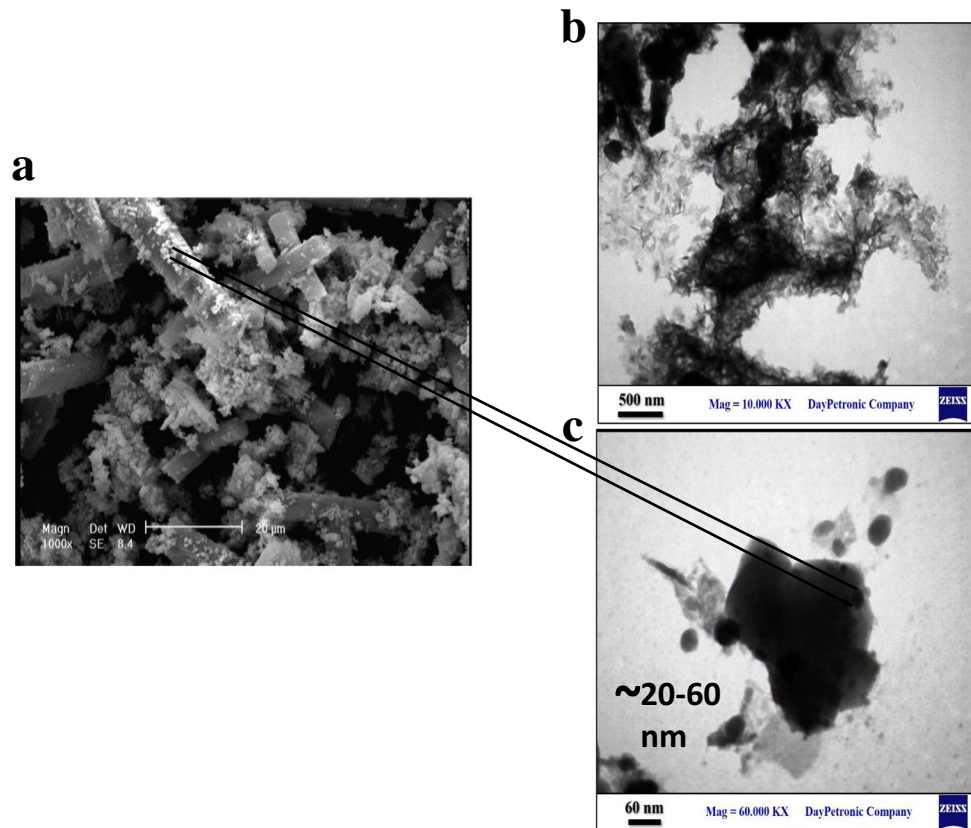


Table 2 ANOVA of the response surface quadratic model for the prediction of the uptake capacity of phosphate

Source	Sum of squares	DF	Mean squares	F-value	p-value
Model	7415.89	14	529.71	24.97	0.00
x_1	1313.59	1	1313.59	61.91	0.00
x_2	717.43	1	717.43	33.81	0.00
x_3	1653.52	1	1653.52	77.94	0.00
x_4	2883.93	1	2883.93	135.93	0.00
x_1^2	2.44	1	2.44	0.11	0.74
x_2^2	70.03	1	70.03	3.3	0.094
x_3^2	205.92	1	205.92	9.71	0.009
x_4^2	17.02	1	17.02	0.8	0.388
$x_1 x_2$	13.5	1	13.5	0.64	0.44
$x_1 x_3$	18.38	1	18.38	0.87	0.37
$x_1 x_4$	47.47	1	47.47	2.24	0.161
$x_2 x_3$	47.47	1	47.47	4.81	0.049
$x_2 x_4$	102.12	1	102.12	2.71	0.126
$x_3 x_4$	57.44	1	57.44	7.8	0.016
Residual	254.6	12	21.22		
Lack of fit	254.6	10	25.46	3.46	0.089
Pure error	0.00	2	0.00		
Cor total	7670.49	26			
Std. dev	4.61		R-sq	96.68%	
PRESS	1466.47		R-sq (adj)	92.81%	
			R-sq (pre)	80.88%	

to Table 2 and Table S2, the F -values of RSM-BBD for q_{eq} and t_s are 24.97 and 54.63, respectively, suggesting the model adequacy fits and significance of predicted responses. However, a greater amount of F -value for t_s confirms the better performance of the model to predict this parameter. Significant model terms for response t_s contain linear effects (x_1, x_2, x_3, x_4) as well as the quadratic effect (x_2^2) while linear effects (x_1, x_2, x_3, x_4), quadratic effect (x_3^2), and interaction effects ($x_2 \times x_3, x_3 \times x_4$) are the significant terms for response q_{eq} . A simpler model can be constructed by removing the non-effective parameters (p -value > 0.05) as follow:

$$t_s = 14.5 - x_1 - 2.5 x_2 + 3.83 x_3 - 1.83 x_4 - 1.083 (x_2)^2 \quad (9)$$

$$q_{eq} = 39.96 + 10.46x_1 - 7.73x_2 - 11.74 x_3 + 15.5 x_4 + 6.21 (x_3)^2 + 5.05(x_2x_3) - 6.43(x_3x_4) \quad (10)$$

For both responses, linear coefficients are more significant than the square and interaction coefficients. It is notable that a significant influence increases by increasing the sum of the squares (see Table 2 and Table S2). A negative sign in Eqs. 7 and 8 shows an antagonistic effect of the variables, which indicates that by increasing these factors, t_s and q_{eq} will decrease. Also, a positive sign shows a synergistic effect, which proposes that by

increasing these factors, t_s and q_{eq} will increase. The initial phosphate concentration, initial solution pH, and influent flow rate have antagonistic effects, whereas bed height has a synergistic effect on t_s . In the case of q_{eq} , initial phosphate concentration, and influent flow rate have synergistic effects, while initial solution pH and bed height have antagonistic effects. It was observed that influent flow rate has the highest effect on the q_{eq} , followed by bed height, initial phosphate concentration, and initial solution pH (see p -value, F -value, and sum of the squares in Table 2). ANOVA results indicated that bed height is the most factor that affected on the t_s , followed by initial solution pH, influent flow rate, and initial phosphate concentration (see p -value, F -value, and sum of the squares in Table S2).

Figure 4 indicates the scatter plot of predicted values of t_s and q_{eq} by the Eqs. 5 and 6, respectively, versus observed values as well as the prediction intervals at 99% level. The results showed that the predicted values by RSM-BBD were in good agreement with the experimental data. The R^2 and R^2_{adj} values for q_{eq} are equal to 96.68% and 92.81%, respectively, and also for t_s are equal to 98.46% and 96.65%, respectively. A decrease of only 3.87% and 1.81% was observed between R^2 and R^2_{adj} for q_{eq} and t_s , respectively, which shows that unnecessary factors have not been included. A lower value of R^2_{adj} compared to R^2 value shows adequate approximation of the experimental data. The values of R^2_{pre} for t_s and q_{eq} were 91.1% and 80.88%, respectively, which propose that the RSM-BBD model can adequately predict the responses. The lack of fit P -value for both responses was greater than 0.05; hence, q_{eq} and t_s are adequately predicted by the quadratic polynomial model and the regression equation was valid for the adsorption of phosphate onto bio-apatite/nZVI composite (Wantala et al. 2012; Maleki and Karimi-Jashni 2020). A lower value of PRESS and standard deviation for t_s in comparison with q_{eq} shows a better fit of the model to predict this parameter.

The normal probability plot of residuals, the plot of residuals versus fitted values, histogram chart of residuals, and plot of residuals versus observations order for both responses are represented in Figs. 5 and S4, which show the effectiveness and reliability of the RSM-BBD model in determining the optimum conditions of q_{eq} and t_s . The data points in the normal probability chart lay on an approximately straight line, which shows the residuals follow a normal distribution (see Figs. 5a and S4a) (Maleki and Karimi-Jashni 2020). A random scatter in the residuals as well as a constant variance of original observations for two responses are represented in Figs. 5b and S4b. The error histogram of residuals implies that the curve is similar to normal (Figs. 5c and S4c). The plot of residuals versus observations order verifies that the residuals fluctuate around the center line, with an interval of ± 8 for q_{eq} and ± 1 for t_s (Figs. 5d and S4d) (Wantala et al. 2012; Amiri et al. 2020a).

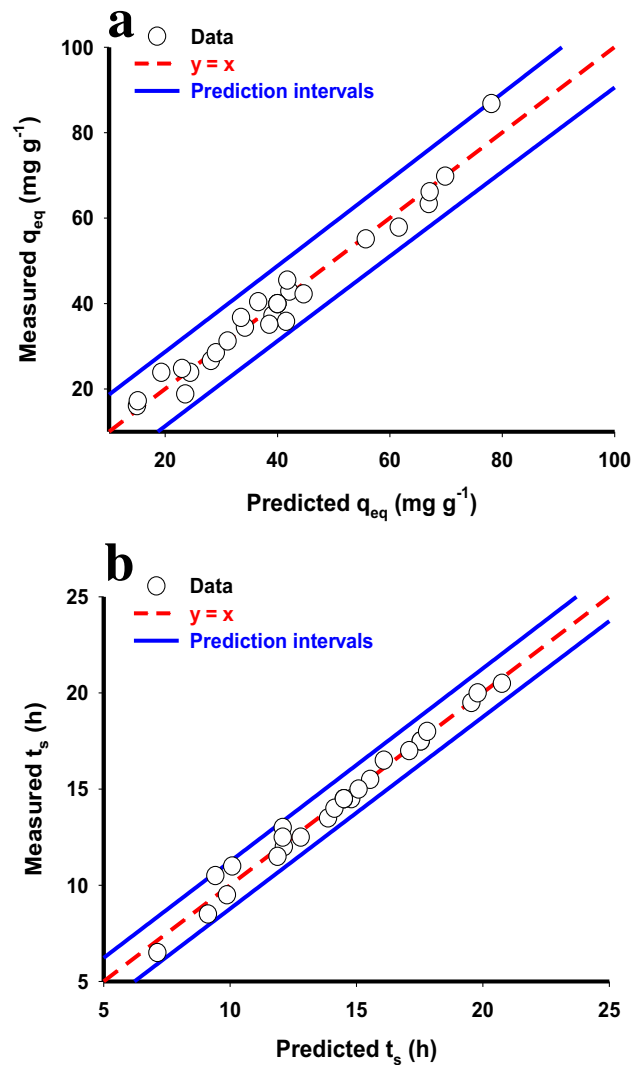


Fig. 4 Scatter plot between measured and predicted values for q_e (a) and t_s (b)

Interactive effect of variables

To study the interactive effects of four variables including initial phosphate concentration, initial solution pH, bed height, and influent flow rate on phosphate uptake capacity by bio-apatite/nZVI composite, contour, and three-dimensional surface plots were constructed. According to ANOVA analysis, the amounts of $\text{prob} > F < 0.05$ show that the significant terms of the quadratic polynomial model are $x_2 \times x_3$ and $x_3 \times x_4$. Therefore, phosphate uptake capacity is plotted as a function of pH and bed height as well as bed height and flow rate, while other remaining variables were kept constant. The contour (see Fig. 6a) and 3D surface (see Fig. 6b) plots of the combined effects of initial solution pH and bed height are represented, while initial phosphate concentration and influent flow rate were

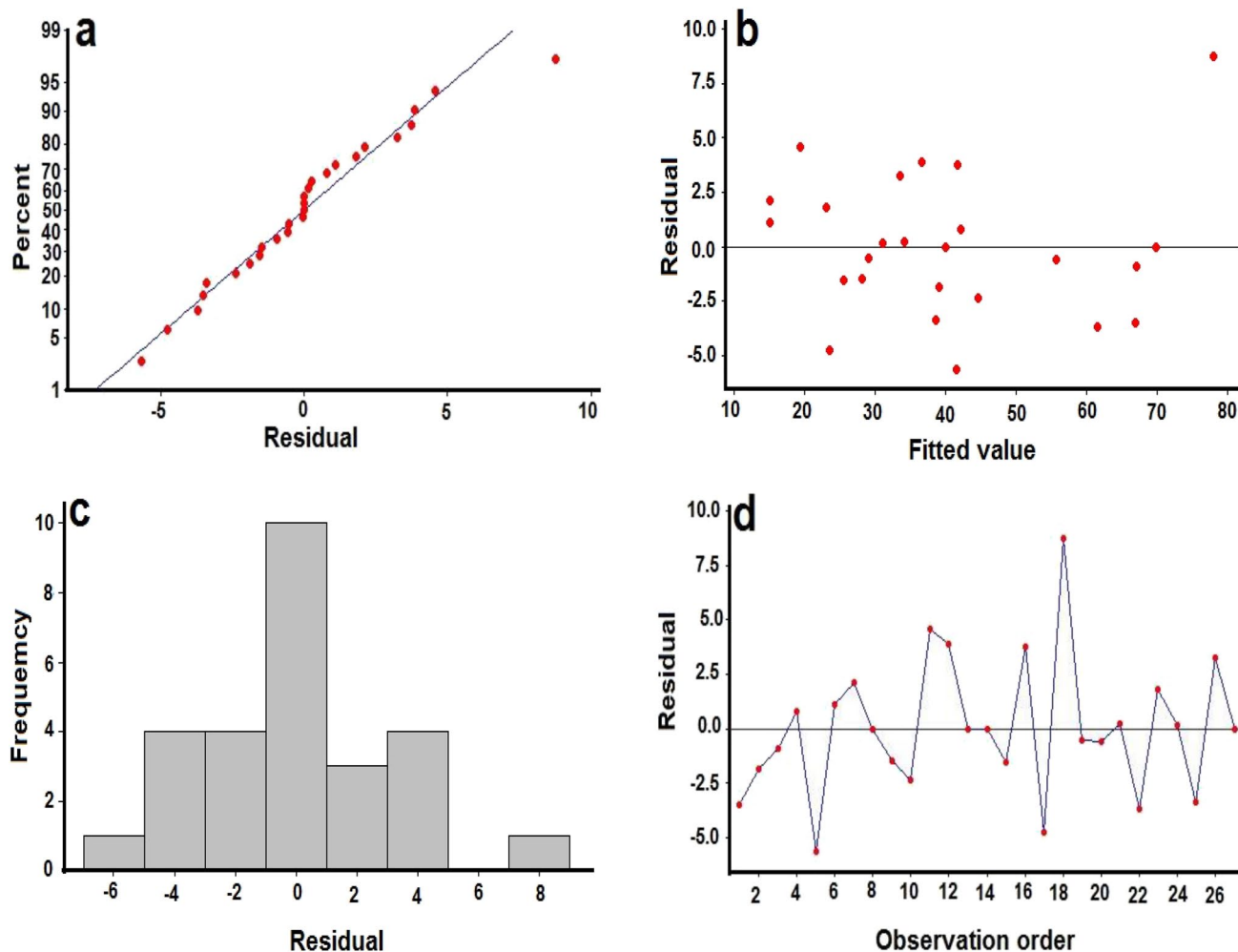


Fig. 5 **a** Normal probability plot of residuals, **b** plot of residuals versus fitted values, **c** histogram chart of residuals, and **d** plot of residuals versus observations order for the uptake capacity of phosphate

kept constant at 150 mg L^{-1} and 5 mL min^{-1} , respectively. It is found that phosphate adsorption capacity increases by decreasing the bed height and pH. As can be seen in Fig. 6a and b, the maximum adsorption capacity of phosphate was observed at pH 2, while gradual and sharp decreases in uptake capacity can be found by increasing the pH from 5 to 8 and pH above 8, respectively. A similar trend was observed by the previous researches (Wen et al. 2014; Arshadi et al. 2015a and 2015b; Malakootian et al. 2018). The phosphate can exist in various forms such as H_3PO_4 , $\text{H}_2\text{PO}_4^{-1}$, and HPO_4^{-2} with $\text{pK}_1 = 2.1$, $\text{pK}_2 = 7.2$, and $\text{pK}_3 = 12.6$, which depend on the pH of the aqueous media. H_3PO_4 , $\text{H}_2\text{PO}_4^{-1}$, and HPO_4^{-2} were the predominant forms of phosphate when the $\text{pH} < 2.1$, $2.1 < \text{pH} < 7.2$, and $7.2 < \text{pH} < 12.6$, respectively (Ma et al. 2020). The influence of pH in phosphate adsorption could be explained by pH_{ZPC} and phosphate species. At $\text{pH} < 5.8$, the surface of the bio-apatite/nZVI composite carries a positive charge

and the adsorbent surface is protonated due to the presence of H^+ species; as a result, the electrostatic interaction between the phosphate anions ($\text{H}_2\text{PO}_4^{-1}$) and the positive charge on the bio-apatite/nZVI composite surfaces increases, which led to increasing the phosphate adsorption capacity. At $\text{pH} > 5.8$, the adsorbent surface is deprotonated due to the presence of OH^- species; thereby, the electrostatic repulsion between the phosphate anions ($\text{H}_2\text{PO}_4^{-1}$ and HPO_4^{-2}) and the negatively charged sites of the bio-apatite/nZVI composite (Fe-OH , $-\text{P-OH}$, and $\equiv\text{Ca-O-H}$ species) increases and consequently the phosphate adsorption capacity decreases (Wen et al. 2014; Arshadi et al. 2015a, b; Malakootian et al. 2018). At $\text{pH} > 8$, the phosphate adsorption capacity is still around $20\text{--}30 \text{ mg g}^{-1}$. It can be understood that electrostatic attraction is not the predominant mechanism, while the coagulation/precipitation process may be a plausible explanation of phosphate adsorption in this pH range (Wen et al. 2014).

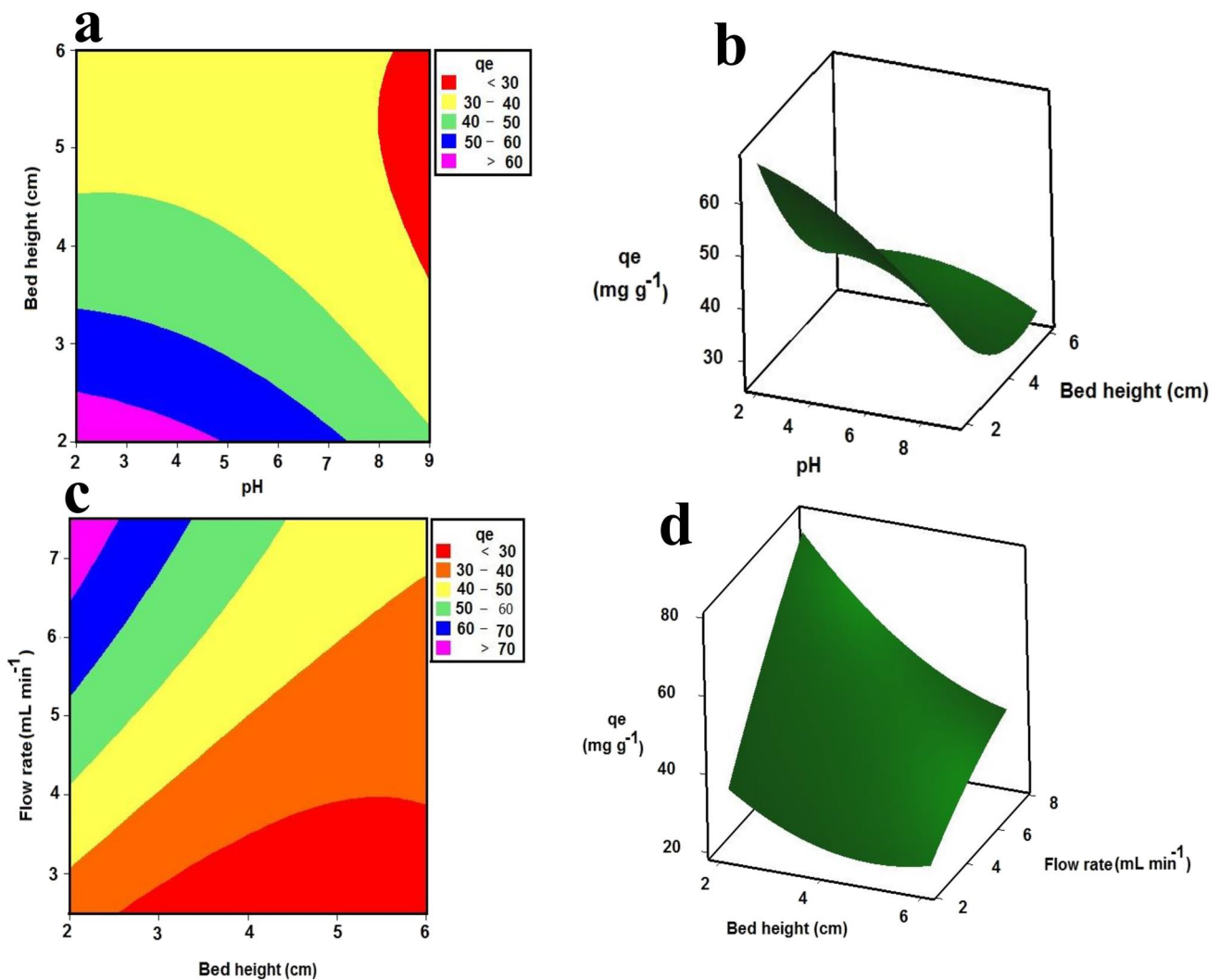


Fig. 6 Contour and surface plots of the q_e as a function of pH and the bed height (a and b) and as a function of the bed height and influent flow rate (c and d)

It was found that when the range of pH was between 2 to 5, the adsorption capacity of phosphate was greater than 60 mg g^{-1} up to bed height 2.5 cm, but at higher bed height, its values gradually decreased. At higher bed depth, the difference between the available adsorption sites and phosphate ions causes most adsorption sites to remain unsaturated, whereas the excess phosphate ions at lower bed depth resulted in the quick saturation of all exposed adsorption sites and consequently faster phosphate-binding on the adsorbent sites (Srivastava et al. 2015). Furthermore, aggregation or agglomeration of bio-apatite/nZVI particles may be occur at higher bed depth, which resulted in a decrease in the available surface area per unit weight (g) of the adsorbent (Srivastava et al. 2015).

The interaction effect of bed height and influent flow rate on the phosphate adsorption capacity is investigated with a constant initial phosphate concentration of 150 mg L^{-1}

and pH of 5.5, which demonstrated that both of the operating factors dramatically affect the adsorption process (see Fig. 6c and d). It is clear that the phosphate adsorption capacity increased by increasing influent flow rate and decreasing bed height. It was found that when the range of bed height was between 4.2 to 6 cm, the phosphate adsorption capacity was lower than 40 mg g^{-1} at flow rate $< 4 \text{ mL min}^{-1}$ and also increased up to 50 mg g^{-1} when the flow rate was greater than 4 mL min^{-1} . However, the highest phosphate adsorption capacity ($> 70 \text{ mg g}^{-1}$) was achieved at flow rate $> 6.5 \text{ mL min}^{-1}$ and bed depth $< 2.5 \text{ cm}$. Increased phosphate adsorption capacity with the increasing amount of influent flow rate is related to more easily penetrating phosphate into the pores of adsorbent. These results indicated that the bio-apatite/nZVI particles can be used as a fixed-bed material for the treatment of phosphate-containing wastewater. A similar behavior has been reported

by Cavas et al. (2011). The sample of the BTC for phosphate adsorption by the bio-apatite/nZVI composite at an initial pollutant concentration of 150 mg L^{-1} , pH of 2, bed height of 6 cm, and influent flow rate of 5 mL min^{-1} is presented in Figure S5.

Process optimization and validation of the model

The main application of the RSM-BBD model is to predict the optimum conditions of various operational factors which affect the elimination of phosphate ions. In this regard, the optimum value for each operating parameter such as initial phosphate concentration, initial solution pH, bed height, and influent flow was predicted by the RSM-BBD model according to the defined domain for the four independent process variables ($100 \text{ mg L}^{-1} < \text{initial phosphate concentration} < 200 \text{ mg}$, $2 < \text{pH} < 9$, $2 \text{ cm} < \text{bed height} < 6 \text{ cm}$, $2.5 \text{ mL min}^{-1} < \text{influent flow rate} < 7.5 \text{ mL min}^{-1}$). Then, the validation of the RSM-BBD was performed by conducting the adsorption experiments in the conditions suggested by the model. The RSM-BBD model predicted maximum phosphate adsorption capacity of 85.71 mg g^{-1} with the desirability of 0.995 under the optimal conditions of 135.35 mg L^{-1} , 2, 2 cm, and 7.5 mL min^{-1} for initial phosphate concentration, initial solution pH, bed height, and influent flow rate, respectively (see Fig. S6a). Furthermore, to determine approximately 19.48 h saturation time, the optimum values of different operational factors were 100 mg L^{-1} initial phosphate concentration, pH 2, bed height 4.46 cm, and influent flow rate 3.1 mL min^{-1} with desirability = 0.998 (see Fig. S6b). More details are presented in supplementary data.

To validate the RSM-BBD model, the predicted responses (q_{eq} and t_s) under optimal values, as suggested by the RSM-BBD model, were also assessed experimentally. It was found that the results of the predicted values using the RSM-BBD model (85.71 mg g^{-1} and 19.48 h) are in good agreement with the laboratory results (84.03 mg g^{-1} , 19.11 h), which implies the validation of the RSM-BBD model.

Fixed-bed adsorption–desorption studies

Regeneration of bio-apatite/nZVI composite is important for its practical usage (Hu et al. 2020). In this regard, a fixed-bed column loaded with bio-apatite/nZVI composite was conducted for five consecutive cycles, and the results are represented in Fig. 7a. The previous researches indicated that 0.1 M NaOH is the most effective eluent for the extraction of adsorbed phosphate ions from stabilized nZVI particles (Arshadi et al. 2015a, b). When NaOH was employed as a desorption agent, the bio-apatite/nZVI surface was abundantly covered by hydroxide ions, which can shift the pH to be higher than 12, and consequently, the phosphate ions with a negative charge will be repelled from the negatively charged bio-apatite/nZVI surface. So, the electrostatic repulsion and competitive force between phosphate and hydroxide ions for adsorption sites will release the phosphate ions from the solid surface into the solution (Almanassra et al. 2020, 2021). It was found that the adsorption efficiency reduced from 97.5 to 76.45%, whereas desorption efficiency reduced from 95.6 to 72.6%, after five adsorption–desorption cycles. Similar findings have been reported by Nodeh et al. (2017) and Huang et al. (2018), which showed that a desorption

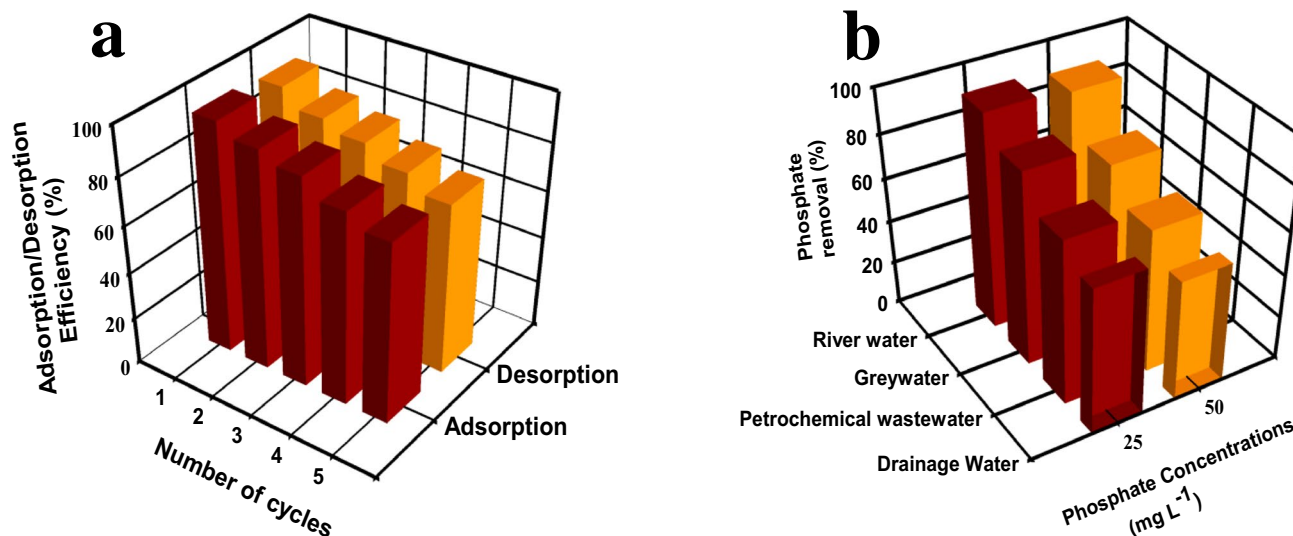


Fig. 7 Effects of consecutive adsorption–desorption cycles on the adsorption/desorption efficiency (a) and removal efficiency of phosphate from real samples (b)

efficiency of over 70% was achieved after 5 adsorption/desorption cycles by NaOH solutions for the extraction of adsorbed phosphate ions. This research showed that the fixed-bed column system with bio-apatite/nZVI composite could be employed for the removal and recovery of phosphate with low losses in its initial adsorption capacity.

Phosphate removal from actual wastewaters

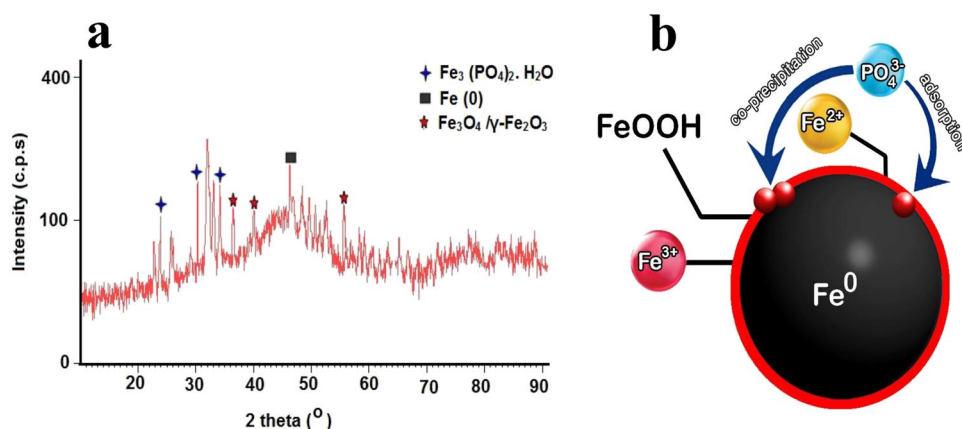
To evaluate the feasibility of large-scale application of bio-apatite/nZVI composite for adsorption of phosphates, the real samples from various sources (river water, agricultural drainage water, greywater, and petrochemical wastewater) were collected and their characteristics are represented in Table S3. After filtering using a 0.45- μm filter membrane, 0.25 g of bio-apatite/nZVI composite was added into 100 mL of sampler containing 25 and 50 mg L^{-1} phosphate, and the removal efficiency of phosphate ions was measured. The removal percentage of phosphate from the real samples was in the order river water > greywater > petrochemical wastewater > agricultural drainage water. As seen in Fig. 7b, the bio-apatite/nZVI composite adsorb more than 98%, 88%, 75%, and 67% of 25 mg L^{-1} phosphate after 120 min from river water, greywater, petrochemical wastewater, and agricultural drainage water samples. When the initial phosphate concentration increased to 50 mg L^{-1} , the removal percentage of phosphate decreased in the same trend from various sources. The adsorption behavior of phosphate from the real samples by bio-apatite/nZVI composite is in accordance with changes in total dissolved solids (TDS). A plausible explanation was that the existence of coexisted anions particularly the divalent anions such as CO_3^{2-} and SO_4^{2-} with a higher charge density can be eliminated faster than phosphate (Luo et al. 2016). In the case of petrochemical wastewater, the initial solution pH (5.1) is lower than pH_{ZPC} (5.7), consequently the electrostatic attraction between $\text{H}_2\text{PO}_4^{-1}$ ions and the positive charges of bio-apatite/nZVI composite might be occur. In the case of river water, greywater, and

drainage water, the initial solution pH is higher than pH_{ZPC} (5.7) (see Table S3), so the electrostatic attraction is not the predominant mechanism. In fact, interaction between phosphate anions and FeOOH lead to incorporation of phosphates in the $\text{Fe}_3(\text{PO}_4)_3$ precipitate structure (Malakootian et al. 2018). So, the coagulation/precipitation reaction is the dominant mechanism for the removal of phosphate in this pH range. So, the bio-apatite/nZVI composite indicates promising potential for phosphate removal from real water.

Phosphate removal mechanism

The nZVI particles have a core-shell structure, in which the shell and core consist of metallic iron and amorphous oxide, respectively (Eslamian et al. 2013). As abovementioned, under acidic conditions ($\text{pH} < \text{pH}_{\text{ZPC}}$), the electrostatic attraction is the main mechanism in phosphate adsorption. However, the ability of bio-apatite/nZVI composite for phosphate adsorption under alkaline conditions ($\text{pH} > \text{pH}_{\text{ZPC}}$) confirms that an additional mechanism other than electrostatic attraction is responsible for the removal of phosphate ions. In this regard, the XRD pattern of bio-apatite/nZVI composite was recorded after impregnation in phosphate solution (see Fig. 8a). The three characteristic peaks at $2\theta = 22.7^\circ$, 29.5° , and 34.1° corresponded to $\text{Fe}_3(\text{PO}_4)_2 \cdot 8\text{H}_2\text{O}$ (vivianite) beside the magnetite/maghemite ($\text{Fe}_3\text{O}_4/\gamma\text{-Fe}_2\text{O}_3$) which are characterized by a $2\theta = 36.6^\circ$, 39.9° , and 55.5° (see Fig. 8a). Similar results were reported by Arshadi et al. (2015a), Arshadi et al. (2015b), and Arshadi et al. (2018). The existence of vivianite in the XRD pattern showed that phosphate was adsorbed on the surface of the bio-apatite/nZVI composite. The same peak for Fe^0 with a lower intensity was observed on the bio-apatite/nZVI surface after phosphate adsorption as compared to the unreacted adsorbent, which shows Fe^0 had not been oxidized entirely. Previous researches demonstrated that iron oxides and hydroxides play an important role in phosphate adsorption (Wen et al. 2014; Arshadi et al. 2018; Maamoun et al. 2018; Malakootian et al. 2018). Therefore, the existence of Fe_2O_3 and Fe_3O_4 on the

Fig. 8 XRD pattern of phosphate loaded on bio-apatite/nZVI composite (a) and phosphate removal mechanisms by bio-apatite/nZVI composite (b)



shell of bio-apatite/nZVI particles after phosphate adsorption combined with the phosphate anions presented in the aqueous media resulting in the co-precipitation of the iron phosphate compounds (see Fig. 8a) (Maamoun et al. 2018). On the other hand, ferric oxyhydrate (FeOOH) was formed under the alkaline condition with an accumulation of hydroxyl ions on the bio-apatite/nZVI composite and interacted with phosphate anion causing incorporation of phosphates in the $\text{Fe}_3(\text{PO}_4)_2$ precipitate structure (Malakootian et al. 2018). Based on the presented results, two main mechanisms for phosphate adsorption by bio-apatite/nZVI composite have been suggested. At low pH, the electrostatic interaction mechanism is dominant, whereas the co-precipitation of Fe and phosphate ions on the bio-apatite/nZVI surface, as well as the chemical adsorption of phosphate on the iron oxy(hydroxide) layer, are dominant at high pH (see Fig. 8b) (Maamoun et al. 2018).

Mathematical model results

The dynamic column experimental data were also fitted to the Thomas and BDST models to study the BTC behavior of phosphate ions by bio-apatite/nZVI composite. The constants for Thomas (K_T and q_0) and BDST (K_{BD} and N_0) models as well as the determination coefficient (R^2) are estimated using non-linear regression analysis. The values of R^2 for the Thomas model range from 98.15 to 99.9 and for BDST range from 94.37 to 95.16 under diverse operating conditions. The results indicated that both models work well for fitting the column experimental data, but the Thomas model performs better in comparison with the BDST model. The average value of q_0 estimated by the Thomas model was 39.12 mg g^{-1} which is close to the experimental value of 40.02 mg g^{-1} . The values of K_T were predicted between $1.6 \times 10^{-4} \text{ L (mg min)}^{-1}$ and $1.9 \times 10^{-4} \text{ L (mg min)}^{-1}$ for various column experiments. These predictions are close to each other with an average value of $1.7 \times 10^{-4} \text{ L (mg min)}^{-1}$ suggesting that column conditions, such as initial phosphate concentration, initial solution pH, bed height, and influent flow rate, have a negligible effect on the BTC. The N_0 values were predicted between 18,146 and 24,275 mg L^{-1} under different experimental conditions. Moreover, the K_{BD} values were found to be in the range of $3.8 \times 10^{-4} \text{ L (mg min)}^{-1}$ and $5.4 \times 10^{-4} \text{ L (mg min)}^{-1}$ for various column experiments, all predictions were close to the mean value, i.e., confirming the application of this model to describe column performance in real condition.

Conclusion

Recycling and separation of bio-apatite-based material are the major problems arising with these materials in wastewater treatment. Moreover, agglomeration, oxidization, low

durability, and poor mechanical of bare nZVI particles are their main challenges for large-scale application in environmental remediation. So, to resolve these limitations, nZVI can be combined with bio-apatite-based material as a supporter due to its low cost, eco-friendly, and easily available. Moreover, from an economic point of view, bio-apatite-based material prepared by the combustion of animal bone could effectively solve the problem of the disposal of animal waste. However, the potential of stabilized nZVI for phosphate removal and recovery from real waters is not well investigated. The phosphate uptake capacity increased with an increase in initial phosphate concentration, and influent flow, and a decrease in initial solution pH and the bed height. Furthermore, the interaction effects of pH and the bed height, as well as the bed height and influent flow rate were significant from the analysis of ANOVA. Under the optimal condition (initial phosphate concentration = 135.35 mg L^{-1} , pH = 2, bed height = 2 cm, and influent flow rate = 7.5 mL min^{-1}), the phosphate adsorption capacity of 85.71 mg g^{-1} was found, which can be explained by more hydroxyl-containing functional groups, high-specific surface area, and more positive zeta potential of adsorbent. The optimum saturation time of 19.48 h was obtained at the initial phosphate concentration of 100 mg L^{-1} , the initial solution pH of 2, the bed height of 4.46 cm, and the influent flow rate of 3.1 mL min^{-1} . High- R^2 and F -values, as well as low probability values, depict the validity of RSM-BBD to predict the q_{eq} and t_s and give suitable information to scale up the column adsorption process. The combined results from column experiments, FTIR spectra, XRD pattern, and pH_{PZC} demonstrated that the possible mechanism was the combination of chemical adsorption, co-precipitation processes, and electrostatic attraction between phosphate anions and the positively charged bio-apatite/nZVI surface under acidic conditions. Findings of the present research propose that bio-apatite/nZVI composite is a versatile and recyclable adsorbent for the removal of phosphate-containing wastewater.

Supplementary Information The online version contains supplementary material available at <https://doi.org/10.1007/s11356-022-20565-8>.

Acknowledgements The authors would like to thank Fasa University for supporting of this work.

Data availability My manuscript has data included as electronic supplementary material.

Declarations

Ethics approval and consent to participate We verify that we have seen and have approved the submitted manuscript. Our manuscript does not report on or involve the use of any animal or human data or tissue.

Competing interests The authors declare no competing interests.

References

- Almanassra IW, Kochkodan V, Mckay G, Kochkodan V, Atieh MA, Al-Ansari T (2020) Review of phosphate removal from water by carbonaceous sorbents. *J Environ Manage* 287:112245
- Almanassra IW, Mckay G, Kochkodan V, Atieh MA, Al-Ansari T (2021) A state of the art review on phosphate removal from water by biochars. *Chem Eng J* 409:128211
- Almeelbi T, Bezbaruah A (2012) Aqueous phosphate removal using nanoscale zero-valent iron. *J Nanoparticle Res* 14:197–210
- Amiri MJ, Abedi-Koupai J, Eslamian SS, Arshadi M (2016) Adsorption of Pb(II) and Hg(II) ions from aqueous single metal solutions by using surfactant-modified ostrich bone waste. *Desalin Water Treat* 57:16522–16539
- Amiri MJ, Abedi-Koupai J, Eslamian SS, Mousavi SF, Hasheminejad H (2013) Modeling Pb(II) adsorption from aqueous solution by ostrich bone ash using adaptive neural-based fuzzy inference system. *J Environ Sci Health Part A* 48(5):543–558
- Amiri MJ, Abedi-koupai J, Eslamian S (2017) Adsorption of Hg(II) and Pb(II) ions by nanoscale zero-valent iron supported on ostrich bone ash in a fixed-bed column system. *Water Sci Technol* 76(3):671–682
- Amiri MJ, Bahrami M, Beigzadeh B, Gil A (2018a) A response surface methodology for optimization of 2,4-dichlorophenoxyacetic acid removal from synthetic and drainage water: a comparative study. *Environ Sci Pollut Res* 25:34277–34293
- Amiri MJ, Bahrami M, Dehkhodaie F (2019) Optimization of Hg(II) adsorption on bio-apatite based materials using CCD-RSM design: characterization and mechanism studies. *J Water Health*. 17:556–567
- Amiri MJ, Mahmoudi MR, Khozaei M (2020a) Fixed bed column modeling of Cd(II) dsorption on bone char using backward Bayesian multiple linear regression. *Pollution* 6:451–461
- Amiri MJ, Roohi R, Gil A (2018b) Numerical simulation of Cd(II) removal by ostrich bone ash supported nanoscale zero-valent iron in a fixed-bed column system: utilization of unsteady advection-dispersion-adsorption equation. *J Water Process Eng* 25:1–14
- Amiri MJ, Roohi R, Arshadi M, Abbaspourrad A (2020b) 2,4-D adsorption from agricultural subsurface drainage by canola stalk-derived activated carbon: insight into the adsorption kinetics models under batch and column conditions. *Environ Sci Pollut Res* 27:16983–16997
- Rice EW, Baird RB, Eaton AD (2017) Standard methods for the examination of water and wastewater, 23st edn. American Public Health Association, Washington, DC, USA
- Arshadi M, EtemadGholtash J, Zandi H, Foroughifard S (2015a) Phosphate removal by a nano-biosorbent from the synthetic and real (Persian Gulf) water samples. *RSC Adv* 5:43290–43302
- Arshadi M, Foroughifard S, EtemadGholtash J, Abbaspourrad A (2015b) Preparation of iron nanoparticles-loaded *Spondias purpurea* seed waste as an excellent adsorbent for removal of phosphate from synthetic and natural waters. *J Colloid Interface Sci* 452:69–77
- Arshadi M, Abdolmaleki MK, Eskandarloo H, Azizi M, Abbaspourrad A (2018) Synthesis of highly monodispersed, stable and spherical NZVI of 20–30 nm on filter paper for the removal of phosphate from wastewater: batch and column study. *ACS Sustain Chem Eng* 6:11662–11676
- Bahrami M, Amiri MJ, Bagheri F (2019) Optimization of the lead removal from aqueous solution using two starch based adsorbents: design of experiments using response surface methodology (RSM). *J Environ Chem Eng* 7:102793
- Bahrami M, Amiri MJ, Beigzadeh B (2018) Adsorption of 2, 4-dichlorophenoxyacetic acid using rice husk biochar, granular activated carbon, and multi-walled carbon nanotubes in a fixed bed column system. *Water Sci Technol* 78:1812–1821
- Cavas L, Karabay Z, Alyuruk H, Dogan H, Demir GK (2011) Thomas and artificial neural network models for the fixed-bed adsorption of methylene blue by a beach waste *Posidonia oceanica* (L.) dead leaves. *Chem Eng J* 171(2):557–562
- Chowdhury S, Saha P (2013) Artificial neural network (ANN) modeling of adsorption of methylene blue by NaOH-modified rice husk in a fixed-bed column system. *Environ Sci Pollut Res* 20(2):1050–1058
- Crane RA, Scott T (2014) The removal of uranium onto carbon-supported nanoscale zero-valent iron particles. *J Nanopart Res* 16:2813
- Cruz-Olivares J, Pérez-Alonso C, Barrera-Díaz C, Ureña-Nuñez F, Chaparro-Mercado MC, Bilyeu B (2013) Modeling of lead (II) biosorption by residue of allspice in a fixed-bed column. *Chem Eng J* 228:21–27
- Eslamian SS, Amiri MJ, Abedi-Koupai J, Shaeri-Karimi S (2013) Reclamation of unconventional water using nano zero-valent iron particles: an application for groundwater. *Int J Water* 7(1/2):1–13
- Gil A, Amiri MJ, Abedi-Koupai J, Eslamian S (2018) Adsorption/reduction of Hg (II) and Pb (II) from aqueous solutions by using bone ash/nZVI composite: effects of aging time, Fe loading quantity and co-existing ions. *Environ Sci Pollut Res* 25:2814–2829
- Gu B-W, Lee C-G, Park S-J (2018) Application of response surface methodology and semi-mechanistic model to optimize fluoride removal using crushed concrete in a fixed-bed column. *Environ Technol* 39:616–627
- Hu A, Ren G, Che J, Guo Y, Ye J, Zhou S (2020) Phosphate recovery with granular acid-activated neutralized red mud: fixed-bed column performance and breakthrough curve modelling. *J Environ Sci* 90:78–86
- Huang Y, Lee X, Macazo FC (2018) A sustainable adsorbent for phosphate removal: modifying multi-walled carbon nanotubes with chitosan. *J Mater Sci* 53:12641–12649
- Li T, Liao T, Su X, Yu X, Han B, Zhu Y, Zhang Y (2018) Preparation of cobalt-containing spinel oxides as novel adsorbents for efficient phosphate removal. *Environ Sci Water Res Technol* 4:1671–1684
- Liu Y, Liu F, Ni L, Meng M, Meng X, Zhong G, Qiu J (2016) A modeling study by response surface methodology (RSM) on Sr(II) ion dynamic adsorption optimization using a novel magnetic ion imprinted polymer. *RSC Adv* 6:54679–54692
- Luo X, Wang X, Bao S, Liu X, Zhang W, Fang T (2016) Adsorption of phosphate in water using one-step synthesised zirconium-loaded reduced graphene oxide. *Sci Rep* 6:1–13
- Ma F, Zhao B, Diao J, Jiang Y, Zhang J (2020) Mechanism of phosphate removal from aqueous solutions by biochar supported nanoscale zero-valent iron. *RSC Adv* 10:39217–39225
- Maamoun I, Eljamal O, Khalil AME, Sugihara Y, Matsunaga N (2018) Phosphate removal through nano-zero-valent iron permeable reactive barrier; column experiment and reactive solute transport modeling. *Transp Porous Media* 125:395–412
- Malakootian M, Daneshkhah M, Hossaini H (2018) Removal of phosphates from aqueous solution by sepiolite-nano zero valent iron composite optimization with response surface methodology. *Int J Environ Sci Technol* 15:2129–2140
- Maleki S, Karimi-Jashni A (2020) Optimization of Ni(II) adsorption onto Cloisite Na⁺ clay using response surface methodology. *Chemosphere* 246:125710
- Mohammad A-T, Abdulhameed AS, Jawad AH (2019) Box-Behnken design to optimize the synthesis of new crosslinked chitosan-glyoxal/TiO₂ nanocomposite: methyl orange adsorption and mechanism studies. *Int J Biol Macromol* 129:98–109
- Nodeh HR, Sereshti H, Afsharian EZ, Nouri N (2017) Enhanced removal of phosphate and nitrate ions from aqueous media using nanosized lanthanum hydrous doped on magnetic graphene nanocomposite. *J Environ Manag* 197:265–274

- Roy S, Das P, Sengupta S (2017) Treatability study using novel activated carbon prepared from rice husk: column study, optimization using response surface methodology and mathematical modeling. *Process Saf Environ Prot* 105:184–193
- Srivastava V, Sharma YC, Sillanpää M (2015) Application of response surface methodology for optimization of Co(II) removal from synthetic wastewater by adsorption on NiO nanoparticles. *J Mol Liq* 211:613–620
- Singh AK, Singh KP (2018) Optimization of phosphate removal from aqueous solution using activated carbon supported zero-valent iron nanoparticles: application of RSM approach. *Appl Water Sci* 8:226
- Wantala K, Khongkasem E, Khlongkarnpanich N, Sthiannopkao S, Kim K-W (2012) Optimization of As(V) adsorption on Fe-RH-MCM-41-immobilized GAC using Box-Behnken design: effects of pH, loadings, and initial concentrations. *Appl Geochemistry* 27:1027–1034
- Wen Z, Zhang Y, Dai C (2014) Removal of phosphate from aqueous solution using nanoscale zerovalent iron (nZVI). *Colloids Surf A Physicochem Eng Asp* 457:433–440
- Wu D, Shen Y, Ding A, Qiu M, Yang Q, Zheng S (2013) Phosphate removal from aqueous solutions by nanoscale zero-valent iron. *Environ Technol* 34:2663–2669
- Yun JH (2000) Unusual adsorber dynamics due to s-shaped equilibrium isotherm. *Korean J Chem Eng* 17:613–617
- Zhang X, Lin S, Chen Z, Megharaj M, Naidu R (2011) Kaolinite-supported nanoscale zero-valent iron for removal of Pb^{2+} from aqueous solution: reactivity, characterization and mechanism. *Water Res* 45:3481–3488
- Zeng H, Lu L, Gong Z, Guo Y, Mo J, Zhang W, Li H (2019) Nanoscale composites of hydroxyapatite coated with zero valent iron: preparation, characterization and uranium removal. *J Radioanal Nucl Chem* 320:165–177

Publisher's note Springer Nature remains neutral with regard to jurisdictional claims in published maps and institutional affiliations.